Geophysical Research Letters

RESEARCH LETTER
10.1029/2024GL110830

Key Points:

- Frictional-viscous flow in a two-phase shear zone modeled by a multiscale approach occurs at ~350–560°C with moderate fluid overpressure
- Stress loading and/or fluid pressure weakening can cause a switch from steady viscous creep to transient frictional slip
- Viscous creep modeled here can accommodate tectonic strain rates but not slow slip events without invoking a switch to frictional sliding

Supporting Information:

Supporting Information may be found in the online version of this article.

Correspondence to:

L. X. Lu,
Xi.Lu@liverpool.ac.uk

Citation:

Lu, L. X., Beall, A., & Fagereng, Å. (2024). Effective bulk rheology of a two-phase subduction shear zone: Insights from micromechanics-based modeling and implications for subduction interface slow slip events. *Geophysical Research Letters*, *51*, e2024GL110830. https://doi.org/10.1029/2024GL110830

Received 14 JUN 2024
Accepted 8 OCT 2024

Effective Bulk Rheology of a Two-Phase Subduction Shear Zone: Insights From Micromechanics-Based Modeling and Implications for Subduction Interface Slow Slip Events

Lucy Xi Lu[1,2], Adam Beall[1,3], and Åke Fagereng[1]

[1]School of Earth and Environmental Sciences, Cardiff University, Cardiff, UK, [2]Department of Earth, Ocean and Ecological Sciences, The University of Liverpool, Liverpool, UK, [3]School of Earth, Atmosphere and Environment, Monash University, Melbourne, VIC, Australia

Abstract Subduction interfaces exhibit various slip styles, including slow slip events (SSEs). We use a micromechanics-based approach to calculate the effective rheology of a shear zone containing ellipsoidal amphibolite clasts deforming by dislocation creep within an interconnected linear-viscous phyllosilicate-dominated matrix. Frictional failure occurs if local stress exceeds Mohr-Coulomb yield strength. At moderate fluid overpressure, mixed-frictional-viscous behavior emerges at ~350–560°C, consistent with a broad zone of mixed fault slip behavior without requiring extreme fluid overpressures. Increasing stress in this transition zone promotes local frictional failure and raises bulk strain rate. If, however, the bulk strain rate increases by more than one order of magnitude, system-wide frictional sliding becomes preferable. This strain rate increase is insufficient to explain the slip rates observed in geophysically detectable SSEs. Therefore, viscous matrix flow as modeled here cannot explain SSEs without either invoking dynamic weakening within a frictional-viscous flow or a mechanism switch to dominantly frictional sliding.

Plain Language Summary Subduction plate boundaries are locked near the Earth's surface and will release the stored energy as earthquakes. Subduction zones creep steadily and viscously at deeper depths where temperatures and pressures are high. At the depth of the transition from earthquakes to steady creep, episodic aseismic slip is often observed. Rocks from this region are mixtures of strong, fractured clasts surrounded by a weak matrix. The observations of exhumed rocks suggest that the episodic, aseismic slip may nucleate when local frictional failure occurs in strong clasts, but the surrounding weak matrix stops this failure from generating major earthquakes. However, it is unclear how much the small-scale rock behavior could be linked to the large-scale slip. We use a numerical model to simulate the interplay between frictional and viscous creep and calculate the overall behavior of the subduction zone plate boundary. We explore how the slip style changes with depth and determine the transition zone's depth/temperature range. In the transition zone, a small increase in stress or decrease in strength can lead to a change from pure viscous flow to frictional sliding. This study overcomes the scale challenge between the small-scale features preserved on outcrops and the large-scale geophysical observations.

1. Introduction

Subduction interfaces slip in variable styles, dominated by earthquakes in a depth-dependent seismogenic zone. The down-dip limit for earthquake nucleation is thought to be controlled by the 350°C isotherm or the upper-plate Moho, whichever is shallower (Hyndman et al., 1997), and represents a transition through a continuum of slip speeds to steady, aseismic sliding at higher temperatures (Peng & Gomberg, 2010). Slow slip events (SSEs) are episodes of transient, aseismic creep at rates of $10^{-7} - 10^{-6}$ ms^{-1}, that most typically occur within this transition zone (Dragert et al., 2001; Peng & Gomberg, 2010). SSEs can be explained by numerical models of a discrete, planar fault with fine-tuned frictional properties at a low effective normal stress based on a rate-and-state-friction framework (Im et al., 2020; Lavier et al., 2013; Liu & Rice, 2005; Rubin, 2008; Skarbek et al., 2012). On the other hand, geological observations and numerical models of more complex fault zones suggest that frictional-viscous interplay may generate SSEs over a larger range of stress conditions (Ando et al., 2012; Beall et al., 2019a, 2019b; Behr et al., 2021; Fagereng & Sibson, 2010; Hayman & Lavier, 2014; Kotowski & Behr, 2019).

Preserved subduction-related shear zones commonly contain cm-to-m-scale brittlely deformed lenses surrounded by an interconnected matrix with ductile deformation structures (Barnes et al., 2020; Fagereng, 2011; Fagereng

et al., 2014; Grigull et al., 2012; Kotowski & Behr, 2019; Phillips et al., 2020). Beall et al. (2019a) modeled a 100 m-wide by 400 m-long heterogeneous shear zone and concluded that fracturing can lead to increased strain rate, but viscous dampening limits acceleration, suppressing earthquake rupture speeds and promoting slower (SSE-style) slip speeds. Numerical models can be scaled up to thicker shear zones with larger clasts (Beall et al., 2019a; Behr et al., 2021; Ioannidi et al., 2021), but the ratio of shear zone length (or width) to clast length (or width) is limited to less than two orders of magnitude. The aspect ratio (length/thickness) of natural faults is therefore inevitably larger than can be captured in detailed fault zone numerical models. Furthermore, geophysically detectable strain rate transients are distributed in multikilometric-scale plate boundary faults (Dragert et al., 2001; Obara et al., 2004; Wallace, 2020), containing heterogeneities at length-scales from micrometers to kilometres, making a case for models that describe multi-scale behavior.

It is still unclear to what extent outcrop-scale heterogeneity inferred from rock records can be linked to variations in plate boundary fault slip style (e.g., Kirkpatrick et al., 2021). Here, we quantify the effective rheology of a heterogeneous subduction thrust interface using a micromechanics-based approach (Figure 1). Jiang (2014) first applied micromechanics to structural geology and proposed a self-consistent MultiOrder Power-Law Approach (MOPLA) for multi-scale deformation and fabric development in Earth's viscous lithosphere. We applied the micromechanics-based approach to a model shear zone consisting of an interconnected low-viscosity matrix containing higher-viscosity clasts. Frictional failure occurs if local stress in a clast or matrix exceeds a Mohr-Coulomb failure strength. We explore how a snapshot of bulk strength and the ratio of frictional to viscous deformation changes with depth along the model subduction interface, and specifically test if a bulk strain rate increase corresponding to SSEs can arise from mixed frictional-viscous flow in response to an instantaneous far-field applied stress.

2. Methodology

Rocks are made of rheologically distinct elements. The macroscale stress and strain rate of the heterogeneous rock mass are, at every point, defined as averages over a Representative Volume Element (RVE, Figure 1b), which contains sufficient distinct elements (k denotes the kth element, $k = 1 \cdots N$) to be a representative sample of the continuum. Local stresses and strain rates may vary from element to element due to distinct rheological properties, shapes and orientations. These local fields are solved according to Eshelby (1957) formalism applied to incompressible viscous materials, treating each element as an ellipsoidal inclusion embedded in infinitely extending homogeneous matrix. The stress/strain rate in the matrix at infinity equals the far-field loading. In this model, we neglect any rate-dependent friction and effectively assume that the viscous matrix dampens any acceleration that may occur in frictionally deforming clasts. We do, however, obtain conditions for when the bulk rheology switches from frictional-viscous flow to system-wide frictional sliding. At this stage the frictional strength of the matrix has been exceeded, but we cannot define the slip speed of the resultant frictional sliding.

To apply Eshelby formalism to a poly-element viscous rock mass with no interconnected matrix, MOPLA defines the idealized homogeneous matrix containing the rest of elements as a reference medium. A specific element's strain rate/stress is solved from the strain rate/stress in the idealized homogeneous matrix. To model the subduction mélange with a clearly identified, interconnected matrix phase ($k = 0$ denotes this matrix phase and $k \geq 1$ denotes clasts, Figure 1c), we use the Mori and Tanaka (1973) scheme that considers the matrix with the existence of other clasts as a reference medium. The strain rate/stress, which is assumed to be uniform in a specific clast, is derived from the average strain rate/stress in the matrix as follows:

$$\dot{\boldsymbol{\varepsilon}}_k = \mathbf{G}_k : \dot{\boldsymbol{\varepsilon}}_0, \quad \mathbf{G}_k = \left[\mathbf{J}^d + \mathbf{S}_k : \left(\mathbf{C}_0^{-1} : \mathbf{C}_k - \mathbf{J}^d\right)\right]^{-1} \tag{1}$$

$$\boldsymbol{\sigma}_k = \mathbf{F}_k : \boldsymbol{\sigma}_0, \quad \mathbf{F}_k = \mathbf{C}_k : \mathbf{G}_k : \mathbf{C}_0^{-1} \tag{2}$$

where $\dot{\boldsymbol{\varepsilon}}_k$ and $\boldsymbol{\sigma}_k$ are local strain rate and deviatoric stress (tensors) in kth phase; if $k = 0$, $\dot{\boldsymbol{\varepsilon}}_0$ and $\boldsymbol{\sigma}_0$ represent the average values in matrix. $\mathbf{C}_k$ is the fourth-order viscosity tensor of kth phase, particularly $\mathbf{C}_0$ is the matrix viscosity. For an isotropic, incompressible fluid, the viscosity tensor becomes a scalar shear viscosity, η (where $\mathbf{C} = 2\eta\mathbf{J}^d$ and $\mathbf{J}^d$ is the fourth-order identity tensor). $\mathbf{G}_k$ and $\mathbf{F}_k$ are *local partitioning tensors*, expressing the local strain rate and stress of kth clast with respect to $\dot{\boldsymbol{\varepsilon}}_0$ and $\boldsymbol{\sigma}_0$. Especially, $\mathbf{G}_0 = \mathbf{J}^d$ and $\mathbf{F}_0 = \mathbf{J}^d$. $\mathbf{S}_k$ is the symmetric

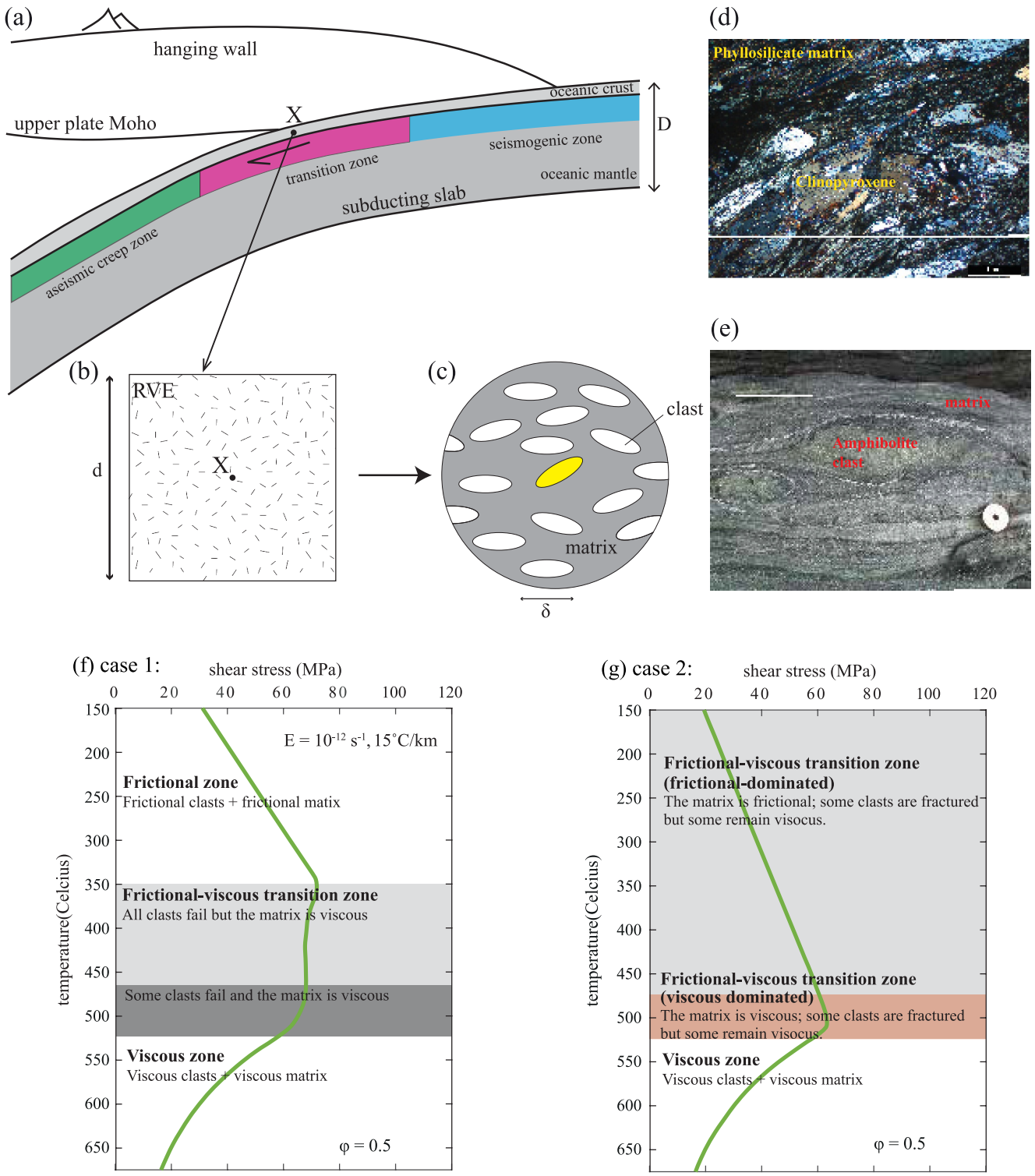

Figure 1. Illustration of the multiscale approach. (a) Schematic subduction interface that shows the gradual frictional-viscous transition separating a seismogenic zone from a deeper aseismic creep zone. (b) Illustrates that the macroscale variables of a shear zone with characteristic length D are defined, centered at point X, in terms of a Representative Volume Element (RVE) with characteristic length d ($D \gg d$). (c) Magnified illustration of an RVE to show a mixture of clasts with a characteristic length of δ ($d \gg \delta$) embedded in an interconnected matrix. The scale separation ($D \gg d \gg \delta$) must be satisfied to apply Eshelby formalism. (d) and (e) are natural examples of competent clasts surrounded by an interconnected, viscous matrix observed under a microscope (d) and in outcrop (e), from the exhumed subduction shear zone in Kyushu, SW Japan (Tulley et al., 2020; Ujiie et al., 2018). (f) and (g) are schematic strength-depth profiles showing the different deformation styles predicted by the model when $\phi = 0.5$. (f) Considers the same friction coefficient for the clasts and matrix (Case 1). (g) Considers different lower friction for the matrix than the clasts (Case 2).

Eshelby tensor of the kth clast (Eshelby, 1957) and depends on clast shape and orientation. The sign: stands for the double-index contracted product operation of two tensors.

The volume average of the local strain rate/stress over the RVE equals the far-field loading: $\mathbf{E} = \sum_{k=0}^{N} \phi_k \dot{\boldsymbol{\varepsilon}}_k$ and $\boldsymbol{\Sigma} = \sum_{k=0}^{N} \phi_k \boldsymbol{\sigma}_k$, with ϕ_k being the volume fraction of kth phase. Therefore, $\dot{\boldsymbol{\varepsilon}}_k$ and $\boldsymbol{\sigma}_k$ are also expressed in terms of $\mathbf{E}$ and $\boldsymbol{\Sigma}$, using the so-called *global partitioning tensors* ($\mathbf{A}$ and $\mathbf{B}$):

$$\dot{\boldsymbol{\varepsilon}}_k = \mathbf{A}_k : \mathbf{E}, \quad \mathbf{A}_k = \mathbf{G}_k \left[\sum_{k=0}^{N} \phi_k \mathbf{G}_k \right]^{-1} \tag{3}$$

$$\boldsymbol{\sigma}_k = \mathbf{B}_k : \boldsymbol{\Sigma}, \quad \mathbf{B}_k = \mathbf{F}_k \left[\sum_{k=0}^{N} \phi_k \mathbf{F}_k \right]^{-1} \tag{4}$$

The effective rheology of the subduction zone is evaluated through the upscaling process of homogenizing the rheological properties of all clasts and matrix over the RVE:

$$\overline{\mathbf{C}} = \sum_{k=0}^{N} \phi_k \mathbf{C}_k \mathbf{G}_k \left[\sum_{l=0}^{N} \phi_l \mathbf{G}_l \right]^{-1} = \sum_{k=0}^{N} \phi_k \mathbf{C}_k \mathbf{A}_k \tag{5}$$

$$\overline{\mathbf{M}} = \sum_{k=0}^{N} \phi_k \mathbf{M}_k \mathbf{F}_k \left[\sum_{l=0}^{N} \phi_l \mathbf{F}_l \right]^{-1} = \sum_{k=0}^{N} \phi_k \mathbf{M}_k \mathbf{B}_k \tag{6}$$

where $\overline{\mathbf{C}}$ and $\overline{\mathbf{M}}$ are the effective viscosity and fluidity (tensors) of the continuum, and inverse of each other. $\mathbf{M}_k$ ($=\mathbf{C}_k^{-1}$) is the fluidity of kth phase. The equations provided above are general expressions for linear materials. We reformulate the non-linear rheology considered here into a pseudo-linear form using a tangent linearization approach (Hutchinson, 1976) to apply above equations to our model (Supplementary Text S1 in Supporting Information S1). The algorithm of this model (model flow chart in Figure S1 in Supporting Information S1) is implemented in MATLAB (Lu et al., 2024).

The strain-rate-related equations (Equations 3 and 5) and stress-related equations (Equations 4 and 6) are equivalent. Therefore one can choose either set depending on whether strain-rate or stress boundary condition is considered. In this study, at local stresses less than the frictional yield strength τ_y, we assume both clasts and matrix are isotropic incompressible fluids; whereas if the local stress equals τ_y, the clast and/or matrix is frictional. τ_y is determined by depth-dependent frictional resistance on existing faults with negligible cohesion:

$$\tau_y = \mu \sigma_n (1 - \lambda) \tag{7}$$

where σ_n is the normal stress on the fault surface, and approximated as the lithostatic pressure P for a gently dipping shear zone in a low differential stress environment (e.g., Lamb, 2006; Wada et al., 2008). λ is the pore pressure factor relating pore fluid pressure $\left(P_f\right)$ and P ($\lambda = P_f/P$), and μ is the friction coefficient. At the yield point, the actual, local strain rate is unknown but the stress is capped by τ_y. Therefore, we consider the stress partitioning under a stress boundary condition throughout this study, using stress-related equations (Equations 4 and 6). We use an effective viscosity η_{eff} to reproduce the yield-point stress state:

$$\tau_y = 2\eta_{eff} \dot{\varepsilon}_{II} \tag{8}$$

where $\dot{\varepsilon}_{II}$ is the second invariant of the local strain rate tensor. η_{eff} and $\dot{\varepsilon}_{II}$ are calculated to satisfy Equation 8 and the far-field loading (Equation 4) through an iteration that terminates when at the local stress coincides with $\tau_y \pm 0.01$ MPa (see Text S2 in Supporting Information S1 and Figure S1 in Supporting Information S1).

Model rheological parameters are informed by geological observations. One example of exhumed subduction-related shear zone is reported in Kyushu, SW Japan, and deformed between ~300°C and ~500°C (Tulley

et al., 2020, 2022; Ujiie et al., 2018), the temperature interval of specific interest for our models, that is, across the thermally controlled frictional-viscous transition. Here, phyllosilicate-dominated metabasalt and metapelite together form the weak matrix deformed predominantly by dissolution-precipitation creep. This weak matrix wraps more competent amphibolite clasts (Figures 1d and 1e). This coexistence of lower-viscosity matrix containing higher-viscosity clasts is widely considered typical for subduction interface fault rocks (e.g., Fagereng & Den Hartog, 2017; Grigull et al., 2012; Kimura et al., 2012; Meneghini et al., 2009; Rowe et al., 2011; Rowe et al., 2013). We therefore model 200 ellipsoidal amphibolite clasts within a phyllosilicate-dominated matrix, deforming by simple shear. As the bulk strength is relatively insensitive to clast shape, size (as long as it is too small to interact with the shear zone boundaries) and orientation (Text S3 in Supporting Information S1 and Figures S2–S4 in Supporting Information S1), for simplicity, all clasts have the same volume fraction, a 3D axial ratio of 3 : 1 : 1, and long axis orientations randomly distributed at angles $\leq 30°$ from the shearing direction. The total clast volume fraction (ϕ) varies from 0.2 to 0.8, but the weak matrix remains interconnected. Within and between exhumed subduction complexes, clast fractions can be spread across this range (Fagereng, 2011; Grigull et al., 2012). Our model could model a shear zone with clasts having different rheological properties and characteristic lengths (Text S3 in Supporting Information S1) but this study only presents the scenario where all clasts have the same rheology and same volume fraction (size). Although we assume that all clasts have the same shape and composition, their local stresses and strain rates vary due to their varied orientations, and differ from the matrix (Figure S5 in Supporting Information S1).

We assume that the phyllosilicate-dominated matrix deforms viscously by dissolution-precipitation creep, based on rock records and experimental and modeling studies (Bos et al., 2000; Bos & Spiers, 2002; Fagereng & Den Hartog, 2017; Rowe et al., 2011; Wassmann & Stöckhert, 2013). In contrast, amphibolite clasts are typically coarser grained and deform viscously by dislocation creep. The clast and matrix viscosity (η) at shear stresses less than τ_y can be expressed in a flow law as (Ranalli, 1995):

$$\eta = \frac{1}{2A}\exp\left(\frac{Q}{RT}\right)\sigma_{II}^{1-n} \tag{9}$$

where σ_{II} is the second invariant of the deviatoric stress tensor, R the gas constant, T the absolute temperate, n the stress exponent, Q the activation energy and A the pre-exponential parameter. For the clasts, we use values (n, Q, and A) for amphibolite from Hacker and Christie (1990). For the matrix, as there is a lack of experimental constraints for dissolution-precipitation creep at natural strain rates, we use $n = 1$, $Q = 35$ kJ/mol, and $A = 1.1 \times 10^{-11}$ MPa^{-1} s^{-1} as extrapolated (see Text S4 in Supporting Information S1) from the field and microstructural study of Tulley et al. (2020).

3. Results

3.1. Strength and Slip Style Variation With Depth

We constructed strength-depth profiles at a representative time-averaged tectonic strain rate of active fault zones $E_{II} = 10^{-12}$ s^{-1} (Fagereng & Biggs, 2019; Lu & Jiang, 2019), a moderate pore pressure factor of $\lambda = 0.8$, and a geothermal gradient of 15°C/km. In Case 1 (Figures 2a–2d), we assume that the friction coefficient for both clasts (μ_c) and matrix (μ_m) is 0.6, a typical 'Byerlee friction' (Byerlee, 1978). At $T < 350$°C, both clasts and matrix fracture and the bulk strength is governed by frictional strength. Frictional-viscous interplay occurs at shear stresses of ~40–90 MPa, less than the yield strength, at ~ 350°C to 500−560°C. In this depth range, local failure occurs in some clasts depending on orientation (Figure S5 in Supporting Information S1) where the local viscous stress attains the yielding strength, but is limited in extent by the viscous matrix. The transition zone depth range becomes greater with increasing ϕ (Figures 2a–2c). The shear stress required to accommodate the imposed strain rate through frictional-viscous behavior also increases with ϕ. At $T > 500-560$°C, depending on ϕ, the subduction interface deforms by steady viscous creep. The bulk strength depends on ϕ and the viscosities of clast and matrix, and decreases with increasing depth/temperature. The ratio of frictional to viscous deformation depends on the number of clasts yielding, and decreases with depth but increases with higher values of ϕ (Figure 2d).

In Case 2 (Figures 2e–2h), we still assume μ_c is 0.6, but assign a weaker μ_m of 0.2, based on both experiments and modeling (e.g., Bos et al., 2000; Bos & Spiers, 2002). A wider frictional-viscous transition zone is produced at $T < 500-560$°C (Figures 2e–2g). The transition zone depth range becomes greater as ϕ increases. The shallower

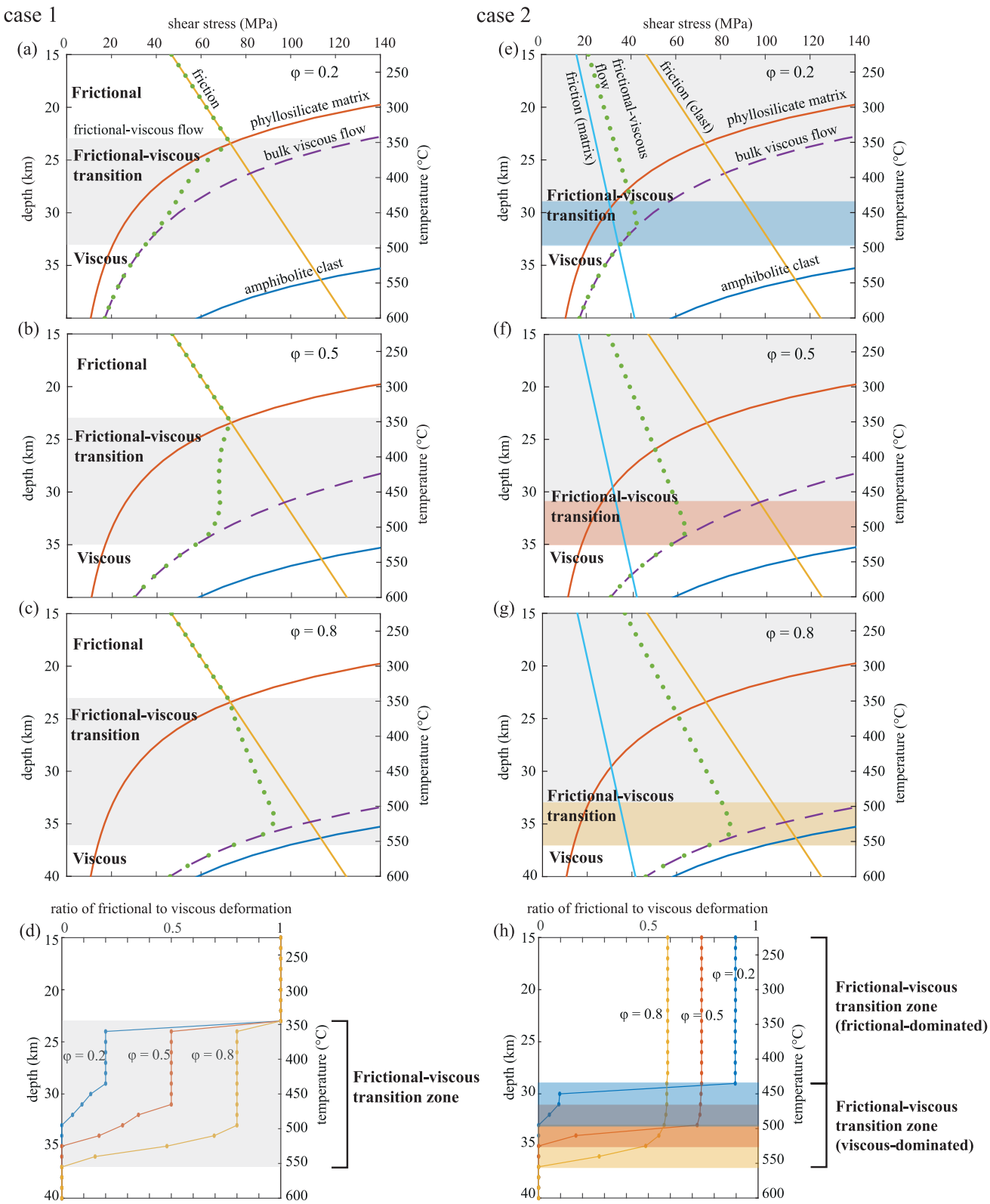
case 1
case 2
shear stress (MPa)
(a)
(b)
(c)
(d)
(e)
(f)
(g)
(h)
φ = 0.2
φ = 0.5
φ = 0.8
Frictional
frictional-viscous flow
Frictional-viscous transition
Viscous
friction
phyllosilicate matrix
bulk viscous flow
amphibolite clast
friction (matrix)
flow
frictional-viscous
friction (clast)
depth (km)
temperature (°C)
ratio of frictional to viscous deformation
Frictional-viscous transition zone
Frictional-viscous transition zone (frictional-dominated)
Frictional-viscous transition zone (viscous-dominated)

Figure 2.

part of the transition zone is frictional-dominated in all cases regardless of ϕ (Figure 2h). In this depth range, the matrix behaves fictionally because μ_m is low, but clasts in some orientations remain viscous because stresses are kept below their yield strength (Figure S5 in Supporting Information S1). The deeper part of the transition zone switches to viscous-dominated as the interconnected matrix becomes viscous (at roughly 29–37 km depth; Figure 2h). Below the transition zone, the shear zone becomes purely viscous.

3.2. The Stress-Strain Rate Relationship in the Frictional-Viscous Transition Zone

We explore how the bulk strain rate and deformation style change with varying driving stresses by running a series of simulations at a fixed depth/temperature (27 km, $T = 405$°C) within the frictional-viscous transition zone we observed in Figure 2, under different shear stresses (Figure 3). We consider the same two cases as above. The pore pressure factor λ varies as 0.8, 0.88 and 0.98.

Broadly, the transition zone is fully viscous at low stresses, and increasing stress leads to bulk viscous strain rate increase accompanied by local frictional failure, until the matrix shear strength is exceeded, allowing system-wide frictional sliding. In Case 1, when the driving stress approaches τ_y, the matrix will have a similar stress state to clasts and close to τ_y (marked by solid circles in Figure 3). The strain rate may increase by more than one order of magnitude with a relatively small increase of the stress before system-wide frictional sliding occurs throughout both matrix and clasts. In Case 2, a small stress change can cause the matrix to become frictional (marked by solid stars in Figure 3) due to a lower yielding strength, and then system-wide frictional sliding occurs but localized to the weaker matrix as stronger clasts may not yield. The strain rate increases by a factor of 1.4–4 before a switch to system-wide frictional failure. Less stress is required for strain rate increase and deformation mechanism change if ϕ is high or τ_y is low. Or in other words, the shear zone is already close to frictional failure because either stress levels are high (because ϕ is high) or high fluid pressure has lowered τ_y.

4. Discussion

4.1. Depth/Temperature-Dependent Rheology of a Multiphase Subduction Thrust Interface

If both clasts and matrix have a friction coefficient of 0.6, and assuming that the frictional regime also represents the seismogenic zone (Scholz, 1988; Sibson, 1983), the model predicts that the base of the seismogenic zone occurs at ∼350°C (24 km, Figures 2a–2c). Below the seismogenic zone, there is a transition zone of mixed frictional-viscous behavior that may represent mixed seismic-aseismic deformation (e.g., Behr & Bürgmann, 2021; Kirkpatrick et al., 2021). The depth and temperature range of the modeled transition zone (Figures 2a–2c) is consistent with geophysically determined, typical deep SSE conditions of 25–50 km and temperatures of 350−550°C (Audet & Kim, 2016; Gao & Wang, 2017), although a frictionally weak matrix allows mixed behavior at shallower depths (Figures 2e–2g). We also find that, at a constant strain rate of 10^{-12} s^{-1}, the behavior in the frictional-viscous transition zone is dominantly viscous if $\phi < 0.5$, and dominantly frictional if $\phi > 0.5$ or μ_m is relatively low (Figures 2d and 2h).

Other studies have also calculated two-phase strength-depth profiles. Handy et al. (1999) proposed a composite flow law for mixtures with interconnected, weak viscous matrix and constructed strength-depth profiles for continental rocks. They predict a relatively narrow frictional-viscous transition zone (∼2 km). The frictional-viscous flow predicted by Handy et al. (1999) is similar to the bulk behavior in our Case 1 if ϕ is low (Figure 2a), but our model predicts a much broader transition zone (∼10 km), particularly in Case 2 where frictional-viscous flow occurs from temperatures well below 300°C. Handy et al. (1999) suggested that the weak nonlinear-viscous matrix governs the bulk rheology even with only 30% matrix material, whereas our model

Figure 2. Model predictions of strength-depth profiles for $\phi = 0.2$, 0.5 and 0.8. (a)–(d) assume $\mu_c = \mu_m = 0.6$ (Case 1). (e)–(h) consider $\mu_c = 0.6$ and $\mu_m = 0.2$ (Case 2). Yellow and light blue lines are frictional strengths with friction coefficients of 0.6 and 0.2, respectively. Red and blue lines are calculated using flow laws of phyllosilicate (Tulley et al., 2020) and amphibolite (Hacker & Christie, 1990), at $E_{II} = 10^{-12}$ s^{-1}. They represent the lower and upper limits, assuming pure phyllosilicate and pure amphibolite, respectively. The bulk strength of the mixture of amphibolite clasts and phyllosilicate matrix is estimated by homogenizing all constituents' rheological properties (Equation 6). The dashed purple line is the bulk strength, without allowing local frictional failure. The dotted green line is the bulk rheology allowing frictional failure when local stresses reach the yield strength. The shaded area illustrates a frictional-viscous transition zone. (d) and (h) show the ratio of frictional to viscous deformation versus depth in both cases.

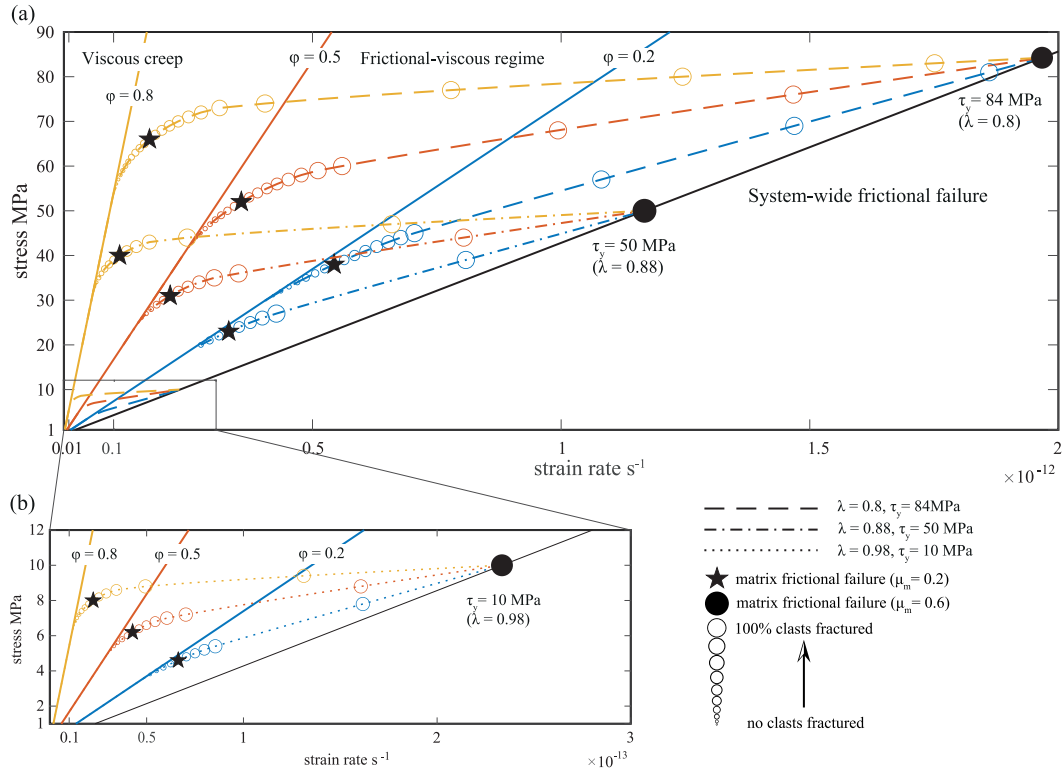

Figure 3. Model predictions of stress-strain rate relationship in the transition zone at 27 km, 405°C The black line represents the matrix rheology with no clasts ($\phi = 0$). Stress-strain rate curves for $\phi = 0.2$, 0.5 and 0.8 are shown in blue, red and yellow colors. Three types of dashed lines for each ϕ correspond to three different pore pressure factors λ of 0.8, 0.88 and 0.98. Solid-colored lines indicate pure viscous creep without any local frictional failure. Dashed-colored lines represent mixed-frictional-viscous behavior. The sizes of the circles show the percentage of fractured clasts. The black circle and black star indicate the moment at which matrix becomes frictional in Case 1 and 2, respectively. (a) Shows all the models, and (b) is a magnification at the stress range of 1–12 MP.a.

predicts that viscous-dominated bulk behavior requires more than 50% viscous matrix. This difference is because we assumed a linear-viscous matrix that cannot accommodate as high strain rates as the nonlinear-viscous matrix assumed by Handy et al. (1999).

Our strength-depth profiles in Case 2 (Figures 2e–2g) are similar to microphysical models of quartz-mica rocks (Bos & Spiers, 2002; Niemeijer & Spiers, 2005). These models suggest a frictional-viscous zone down to 15–20 km depth, and that its behavior could be approximated by an apparent friction coefficient of 0.12–0.35 (Bos & Spiers, 2002). The bulk strengths in these models are greater than our estimates, because they used a smaller pore fluid factor of 0.36. Fagereng and Den Hartog (2017) also used a microphysical model of quartz-mica rocks but considered moderate and high pore fluid pressures ($\lambda = 0.8$ and 0.95) and suggests a lower stress of ≤ 20 MPa for frictional-viscous flow. Elevated pore pressure at the base of the subduction seismogenic zone is expected according to geophysical and geologic observations (e.g., Condit & French, 2022; Rowe et al., 2009; Saffer & Tobin, 2011). Therefore our model with $\lambda = 0.8$ better reflects the real subduction fault. Overall, our model results are within the range of past studies but show a general case for a fault zone governed by dissolution-precipitation creep in phyllosilicate-rich matrix enveloping higher viscosity lenses with a dislocation creep or frictional rheology (e.g., Tulley et al., 2020; Wassmann & Stöckhert, 2013).

4.2. Stress/Strain Rate-Dependent Rheology of the Heterogeneous Subduction Zone Interface

The deformation mechanism of the heterogeneous subduction thrust interface switches from steady viscous creep to frictional slip after a stress perturbation that depends on ϕ and τ_y but is generally small relative to bulk stress (Figure 3). Models for SSEs in heterogeneous shear zones (Behr et al., 2021; Skarbek et al., 2012) assume small effective stresses, for example, less than 6 MPa in Skarbek et al. (2012). Here, we suggest that under a relatively

wide range of conditions, a stress increase of 1.6–64 MPa (depending on ϕ and τ_y) can increase bulk strain rate and change bulk behavior (Figure 3). This range of stresses would be compatible with interpreting low seismic velocities as resulting from other factors than high fluid pressure, such as presence of a well-developed fabric (Miller et al., 2021).

Our models, invoking local stresses exceeding yield strengths as a trigger for a larger (up to multikilometer) scale deformation mechanism switch, are comparable to the outcrop-scale models of Beall et al. (2019a), who suggested the development of a force chain network extending the whole shear zone for clast-rich cases ($\phi > 0.5$). When the stress-bearing clasts undergo frictional failure, the stress in the force chain network is damped into the viscous matrix, and the bulk strain rate is consistent with SSEs when the matrix viscosity is 10^{16}–10^{18} Pa s. Our models predict that regardless of ϕ and pore fluid pressure/yield strength, increasing driving stress leads to frictional failure in clasts/matrix and an increase in bulk strain rate. If ϕ is high or τ_y is low, clasts are easier to fail, and a smaller stress change is required for a bulk strain rate increase and deformation mechanism change.

4.3. Consequences for Possible Slow Slip Mechanisms

Local increase in fluid pressure has been suggested as an SSE triggering mechanism (e.g., Gosselin et al., 2020; Warren-Smith et al., 2019). In our models, increased fluid pressure decreases τ_y, promoting local frictional failure, and system-wide frictional sliding if stress is sufficiently high (Figure 3). At the point of system-wide frictional failure, the shear zone rheology is controlled by dynamic frictional properties that are not included in our model, so whether the mechanism change leads to earthquake slip speeds or slower forms of transient slip is unclear.

While the models we present here do not quantify slip rate during system-wide frictional sliding, they can predict increases in frictional-viscous strain rates where the local frictional sliding is dampened by the surrounding, viscous matrix. The bulk viscous strain rate may increase up to $2 \times 10^{-12}\text{s}^{-1}$ before frictional sliding becomes preferable (Figure 3), which seems too slow to explain SSEs ($10^{-11} - 10^{-10}\text{s}^{-1}$ for a 100 m thick shear zone). Previous models suggested a matrix viscosity near 10^{18} Pa s or smaller ($10^{16} - 10^{18}$ Pa s) combined with high ϕ could allow for potential SSEs by a viscous mechanism (Beall et al., 2019a; Behr et al., 2021). We used a field-based flow law for the phyllosilicate matrix, and the matrix viscosity is $\sim 2 \times 10^{19}$ Pa s at 27 km and 405°C, higher than in the other studies. The field constraint is based on paleopiezometry, which has some intrinsic uncertainty in the calibration, and may also be an upper limit because it is based on a relatively strong deformed quartz phase (Tulley et al., 2020). Variation in measured grain sizes also gives a range in calculated viscosity at a given depth of about an order of magnitude (Tulley et al., 2020). If we consider a matrix viscosity 10 times weaker, the maximum viscous strain rate accompanied by local, but not system-wide, frictional failure becomes around 10 times faster (Figure S8 in Supporting Information S1); however, the strain rate increase before system-wide fictional failure is always at most one order of magnitude, because lowering the matrix viscosity also tends to reduce the bulk strength in pure viscous creep regime.

Our model with a linear-viscous matrix rheology is inconsistent with the hypothesis that slow slip can be transient, high strain-rate, viscous creep driven by a stress increase (Fagereng et al., 2014; Hayman & Lavier, 2014). As in our models, a field-based study by Condit et al. (2022) concluded that dissolution-precipitation creep is efficient at accommodating tectonic strain rates, but cannot, alone, accommodate slow slip rates. In their and our models, a switch to a frictional rheology is required for SSEs, and a minimum requirement is that conditions for such a switch are reached. It could, however, be possible for a different rheology, for example, the nonlinear-viscous flow of interconnected layers of muscovite or biotite, to achieve slow slip rates under small driving stresses (Fagereng et al., 2014). Alternatively, a viscous-frictional mechanism for SSEs is also feasible if the localized frictional component undergoes some modest rate-weakening (Beall et al., 2019a; Behr et al., 2021). For example, our model only estimates the average stress level in the matrix, a simplification that neglects any contribution of localized frictional deformation in the matrix and associated effects on bulk behavior.

5. Conclusion

We considered a subduction mélange with amphibolite clasts embedded in an interconnected phyllosilicate matrix and used the Mori-Tanaka (Mori & Tanaka, 1973) scheme to model multiphase bulk rheology in a micromechanics-based approach (MOPLA, Jiang, 2014). The model predicts a wide frictional-viscous transition

zone where the competent clasts fracture but the frictional sliding is limited by a viscous, weak matrix at shear stresses of approximately 40–90 MPa, less than the yield strength at moderate fluid overpressure, at ~350°C to 500–560°C. In this transition zone, a shear stress increase of 1.6–64 MPa can switch the deformation mechanism from dominantly viscous to locally frictional and finally to system-wide frictional failure. If the fluid pressure increases and thus decrease the τ_y, or the stress levels are high because of high ϕ, less stress change would lead to a deformation style switch. Heterogeneities promote the switch in deformation style. In a viscous shear zone controlled by the dissolution-precipitation creep flow law used here, the frictional-viscous flow can accommodate a bulk strain rate increase up to one order of magnitude - but larger strain rate requires a complete, but transient, switch to frictional behavior. In this model and choice of rheology, SSEs require frictional sliding and cannot be explained by fast viscous flow alone.

Data Availability Statement

No data were used or produced in this manuscript. The MATLAB code (Lu et al., 2024) used for our models is available here: https://github.com/geolucyxlu/2phase-frictional-viscous-model (10.5281/zenodo.13319255).

Acknowledgments
This project has received funding from the European Research Council (ERC) under the European Union's Horizon 2020 research and innovation program (starting grant agreement 715836 MICA).

References

Ando, R., Takeda, N., & Yamashita, T. (2012). Propagation dynamics of seismic and aseismic slip governed by fault heterogeneity and Newtonian rheology. *Journal of Geophysical Research*, *117*(B11). https://doi.org/10.1029/2012jb009532

Audet, P., & Kim, Y. (2016). Teleseismic constraints on the geological environment of deep episodic slow earthquakes in subduction zone forearcs: A review. *Tectonophysics*, *670*, 1–15. https://doi.org/10.1016/j.tecto.2016.01.005

Barnes, P. M., Wallace, L. M., Saffer, D. M., Bell, R. E., Underwood, M. B., Fagereng, A., et al. (2020). Slow slip source characterized by lithological and geometric heterogeneity. *Science Advances*, *6*(13), eaay3314. https://doi.org/10.1126/sciadv.aay3314

Beall, A., Fagereng, Å., & Ellis, S. (2019a). Fracture and weakening of jammed subduction shear zones, leading to the generation of slow slip events. *Geochemistry, Geophysics, Geosystems*, *20*(11), 4869–4884. https://doi.org/10.1029/2019gc008481

Beall, A., Fagereng, Å., & Ellis, S. (2019b). Strength of strained two-phase mixtures: Application to rapid creep and stress amplification in subduction zone mélange. *Geophysical Research Letters*, *46*(1), 169–178. https://doi.org/10.1029/2018gl081252

Behr, W. M., & Bürgmann, R. (2021). What's down there? The structures, materials and environment of deep-seated slow slip and tremor. *Philosophical Transactions of the Royal Society A*, *379*(2193), 20200218. https://doi.org/10.1098/rsta.2020.0218

Behr, W. M., Gerya, T. V., Cannizzaro, C., & Blass, R. (2021). Transient slow slip characteristics of frictional-viscous subduction megathrust shear zones. *AGU Advances*, *2*(3), e2021AV000416. https://doi.org/10.1029/2021av000416

Bos, B., Peach, C., & Spiers, C. (2000). Frictional-viscous flow of simulated fault gouge caused by the combined effects of phyllosilicates and pressure solution. *Tectonophysics*, *327*(3–4), 173–194. https://doi.org/10.1016/s0040-1951(00)00168-2

Bos, B., & Spiers, C. J. (2002). Frictional-viscous flow of phyllosilicate-bearing fault rock: Microphysical model and implications for crustal strength profiles. *Journal of Geophysical Research*, *107*(B2), ECV–1. https://doi.org/10.1029/2001jb000301

Byerlee, J. D. (1978). Friction of rocks. *Pure and Applied Geophysics*, *116*, 615–626. https://doi.org/10.1007/978-3-0348-7182-2_4

Condit, C. B., & French, M. E. (2022). Geologic evidence of lithostatic pore fluid pressures at the base of the subduction seismogenic zone. *Geophysical Research Letters*, *49*(12), e2022GL098862. https://doi.org/10.1029/2022gl098862

Condit, C. B., French, M. E., Hayles, J. A., Yeung, L. Y., Chin, E. J., & Lee, C.-T. A. (2022). Rheology of metasedimentary rocks at the base of the subduction seismogenic zone. *Geochemistry, Geophysics, Geosystems*, *23*(2), e2021GC010194. https://doi.org/10.1029/2021gc010194

Dragert, H., Wang, K., & James, T. S. (2001). A silent slip event on the deeper cascadia subduction interface. *Science*, *292*(5521), 1525–1528. https://doi.org/10.1126/science.1060152

Eshelby, J. D. (1957). The determination of the elastic field of an ellipsoidal inclusion, and related problems. *Proceedings of the Royal Society of London - Series A: Mathematical and Physical Sciences*, *241*(1226), 376–396.

Fagereng, Å. (2011). Frequency-size distribution of competent lenses in a block-in-matrix mélange: Imposed length scales of brittle deformation? *Journal of Geophysical Research*, *116*(B5), B05302. https://doi.org/10.1029/2010jb007775

Fagereng, Å., & Biggs, J. (2019). New perspectives on 'geological strain rates' calculated from both naturally deformed and actively deforming rocks. *Journal of Structural Geology*, *125*, 100–110. https://doi.org/10.1016/j.jsg.2018.10.004

Fagereng, Å., & Den Hartog, S. A. (2017). Subduction megathrust creep governed by pressure solution and frictional–viscous flow. *Nature Geoscience*, *10*(1), 51–57. https://doi.org/10.1038/ngeo2857

Fagereng, Å., Hillary, G. W., & Diener, J. F. (2014). Brittle-viscous deformation, slow slip, and tremor. *Geophysical Research Letters*, *41*(12), 4159–4167. https://doi.org/10.1002/2014gl060433

Fagereng, Å., & Sibson, R. H. (2010). Melange rheology and seismic style. *Geology*, *38*(8), 751–754. https://doi.org/10.1130/g30868.1

Gao, X., & Wang, K. (2017). Rheological separation of the megathrust seismogenic zone and episodic tremor and slip. *Nature*, *543*(7645), 416–419. https://doi.org/10.1038/nature21389

Gosselin, J. M., Audet, P., Estève, C., McLellan, M., Mosher, S. G., & Schaeffer, A. J. (2020). Seismic evidence for megathrust fault-valve behavior during episodic tremor and slip. *Science Advances*, *6*(4), eaay5174. https://doi.org/10.1126/sciadv.aay5174

Grigull, S., Krohe, A., Moos, C., Wassmann, S., & Stöckhert, B. (2012). "order from chaos": A field-based estimate on bulk rheology of tectonic mélanges formed in subduction zones. *Tectonophysics*, *568*, 86–101. https://doi.org/10.1016/j.tecto.2011.11.004

Hacker, B. R., & Christie, J. M. (1990). Brittle/ductile and plastic/cataclastic transitions in experimentally deformed and metamorphosed amphibolite. In *The Brittle-Ductile Transition in Rocks* (Vol. 56, pp. 127–147). https://doi.org/10.1029/gm056p0127

Handy, M., Wissing, S., & Streit, L. (1999). Frictional–viscous flow in mylonite with varied bimineralic composition and its effect on lithospheric strength. *Tectonophysics*, *303*(1–4), 175–191. https://doi.org/10.1016/s0040-1951(98)00251-0

Hayman, N. W., & Lavier, L. L. (2014). The geologic record of deep episodic tremor and slip. *Geology*, *42*(3), 195–198. https://doi.org/10.1130/g34990.1

Hutchinson, J. W. (1976). Bounds and self-consistent estimates for creep of polycrystalline materials. *Proceedings of the Royal Society of London. A. Mathematical and Physical Sciences*, *348*(1652), 101–127.
Hyndman, R. D., Yamano, M., & Oleskevich, D. A. (1997). The seismogenic zone of subduction thrust faults. *Island Arc*, *6*(3), 244–260. https://doi.org/10.1111/j.1440-1738.1997.tb00175.x
Im, K., Saffer, D., Marone, C., & Avouac, J.-P. (2020). Slip-rate-dependent friction as a universal mechanism for slow slip events. *Nature Geoscience*, *13*(10), 705–710. https://doi.org/10.1038/s41561-020-0627-9
Ioannidi, P. I., Le Pourhiet, L., Agard, P., Angiboust, S., & Oncken, O. (2021). Effective rheology of a two-phase subduction shear zone: Insights from numerical simple shear experiments and implications for subduction zone interfaces. *Earth and Planetary Science Letters*, *566*, 116913. https://doi.org/10.1016/j.epsl.2021.116913
Jiang, D. (2014). Structural geology meets micromechanics: A self-consistent model for the multiscale deformation and fabric development in earth's ductile lithosphere. *Journal of Structural Geology*, *68*, 247–272. https://doi.org/10.1016/j.jsg.2014.05.020
Kimura, G., Yamaguchi, A., Hojo, M., Kitamura, Y., Kameda, J., Ujiie, K., et al. (2012). Tectonic mélange as fault rock of subduction plate boundary. *Tectonophysics*, *568*, 25–38. https://doi.org/10.1016/j.tecto.2011.08.025
Kirkpatrick, J. D., Fagereng, Å., & Shelly, D. R. (2021). Geological constraints on the mechanisms of slow earthquakes. *Nature Reviews Earth and Environment*, *2*(4), 285–301. https://doi.org/10.1038/s43017-021-00148-w
Kotowski, A. J., & Behr, W. M. (2019). Length scales and types of heterogeneities along the deep subduction interface: Insights from exhumed rocks on syros island, Greece. *Geosphere*, *15*(4), 1038–1065. https://doi.org/10.1130/ges02037.1
Lamb, S. (2006). Shear stresses on megathrusts: Implications for mountain building behind subduction zones. *Journal of Geophysical Research*, *111*(B7). https://doi.org/10.1029/2005jb003916
Lavier, L. L., Bennett, R. A., & Duddu, R. (2013). Creep events at the brittle ductile transition. *Geochemistry, Geophysics, Geosystems*, *14*(9), 3334–3351. https://doi.org/10.1002/ggge.20178
Liu, Y., & Rice, J. R. (2005). Aseismic slip transients emerge spontaneously in three-dimensional rate and state modeling of subduction earthquake sequences. *Journal of Geophysical Research*, *110*(B8). https://doi.org/10.1029/2004jb003424
Lu, L. X., Beall, A., & Fagereng, A. (2024). 2phase-frictional-viscous-model: August 14, 2024 release (version 1.0.0). *Zenodo*. [Software]. https://doi.org/10.5281/zenodo.13319255
Lu, L. X., & Jiang, D. (2019). Quartz flow law revisited: The significance of pressure dependence of the activation enthalpy. *Journal of Geophysical Research: Solid Earth*, *124*(1), 241–256. https://doi.org/10.1029/2018jb016226
Meneghini, F., Marroni, M., Moore, J. C., Pandolfi, L., & Rowe, C. D. (2009). The record of underthrusting and underplating in the geologic record: Structural diversity between the franciscan complex (California), the kodiak complex (Alaska) and the internal ligurian units (Italy). *Geological Journal*, *44*(2), 126–152. https://doi.org/10.1002/gj.1144
Miller, P. K., Saffer, D. M., Abers, G. A., Shillington, D. J., Bécel, A., Li, J., & Bate, C. (2021). P- and s-wave velocities of exhumed metasediments from the alaskan subduction zone: Implications for the in situ conditions along the megathrust. *Geophysical Research Letters*, *48*(20), e2021GL094511. https://doi.org/10.1029/2021GL094511
Mori, T., & Tanaka, K. (1973). Average stress in matrix and average elastic energy of materials with misfitting inclusions. *Acta Metallurgica*, *21*(5), 571–574. https://doi.org/10.1016/0001-6160(73)90064-3
Niemeijer, A. R., & Spiers, C. J. (2005). Influence of phyllosilicates on fault strength in the brittle-ductile transition: Insights from rock analogue experiments. *Geological Society, London, Special Publications*, *245*(1), 303–327. https://doi.org/10.1144/gsl.sp.2005.245.01.15
Obara, K., Hirose, H., Yamamizu, F., & Kasahara, K. (2004). Episodic slow slip events accompanied by non-volcanic tremors in southwest Japan subduction zone. *Geophysical Research Letters*, *31*(23). https://doi.org/10.1029/2004gl020848
Peng, Z., & Gomberg, J. (2010). An integrated perspective of the continuum between earthquakes and slow-slip phenomena. *Nature Geoscience*, *3*(9), 599–607. https://doi.org/10.1038/ngeo940
Phillips, N. J., Motohashi, G., Ujiie, K., & Rowe, C. D. (2020). Evidence of localized failure along altered basaltic blocks in tectonic mélange at the updip limit of the seismogenic zone: Implications for the shallow slow earthquake source. *Geochemistry, Geophysics, Geosystems*, *21*(7), e2019GC008839. https://doi.org/10.1029/2019gc008839
Ranalli, G. (1995). *Rheology of the earth*. Springer Science and Business Media.
Rowe, C. D., Meneghini, F., & Moore, J. C. (2009). Fluid-rich damage zone of an ancient out-of-sequence thrust, kodiak islands, Alaska. *Tectonics*, *28*(1). https://doi.org/10.1029/2007tc002126
Rowe, C. D., Meneghini, F., & Moore, J. C. (2011). Textural record of the seismic cycle: Strain-rate variation in an ancient subduction thrust. *Geological Society, London, Special Publications*, *359*(1), 77–95. https://doi.org/10.1144/sp359.5
Rowe, C. D., Moore, J., & Remitti, F., & IODP Expedition 343/343T Scientists. (2013). The thickness of subduction plate boundary faults from the seafloor into the seismogenic zone. *Geology*, *41*(9), 991–994. https://doi.org/10.1130/g34556.1
Rubin, A. M. (2008). Episodic slow slip events and rate-and-state friction. *Journal of Geophysical Research*, *113*(B11). https://doi.org/10.1029/2008jb005642
Saffer, D. M., & Tobin, H. J. (2011). Hydrogeology and mechanics of subduction zone forearcs: Fluid flow and pore pressure. *Annual Review of Earth and Planetary Sciences*, *39*(1), 157–186. https://doi.org/10.1146/annurev-earth-040610-133408
Scholz, C. (1988). The brittle-plastic transition and the depth of seismic faulting. *Geologische Rundschau*, *77*(1), 319–328. https://doi.org/10.1007/bf01848693
Sibson, R. H. (1983). Continental fault structure and the shallow earthquake source. *Journal of the Geological Society*, *140*(5), 741–767. https://doi.org/10.1144/gsjgs.140.5.0741
Skarbek, R. M., Rempel, A. W., & Schmidt, D. A. (2012). Geologic heterogeneity can produce aseismic slip transients. *Geophysical Research Letters*, *39*(21). https://doi.org/10.1029/2012gl053762
Tulley, C. J., Fagereng, Å., & Ujiie, K. (2020). Hydrous oceanic crust hosts megathrust creep at low shear stresses. *Science Advances*, *6*(22), eaba1529. https://doi.org/10.1126/sciadv.aba1529
Tulley, C. J., Fagereng, Å., Ujiie, K., Diener, J. F. A., & Harris, C. (2022). Embrittlement within viscous shear zones across the base of the subduction thrust seismogenic zone. *Geochemistry, Geophysics, Geosystems*, *23*(9). https://doi.org/10.1029/2021gc010208
Ujiie, K., Saishu, H., Fagereng, Å., Nishiyama, N., Otsubo, M., Masuyama, H., & Kagi, H. (2018). An explanation of episodic tremor and slow slip constrained by crack-seal veins and viscous shear in subduction mélange. *Geophysical Research Letters*, *45*(11), 5371–5379. https://doi.org/10.1029/2018gl078374
Wada, I., Wang, K., He, J., & Hyndman, R. D. (2008). Weakening of the subduction interface and its effects on surface heat flow, slab dehydration, and mantle wedge serpentinization. *Journal of Geophysical Research*, *113*(B4). https://doi.org/10.1029/2007jb005190

Wallace, L. M. (2020). Slow slip events in New Zealand. *Annual Review of Earth and Planetary Sciences*, *48*(1), 175–203. https://doi.org/10.1146/annurev-earth-071719-055104

Warren-Smith, E., Fry, B., Wallace, L., Chon, E., Henrys, S., Sheehan, A., et al. (2019). Episodic stress and fluid pressure cycling in subducting oceanic crust during slow slip. *Nature Geoscience*, *12*(6), 475–481. https://doi.org/10.1038/s41561-019-0367-x

Wassmann, S., & Stöckhert, B. (2013). Rheology of the plate interface—Dissolution precipitation creep in high pressure metamorphic rocks. *Tectonophysics*, *608*, 1–29. https://doi.org/10.1016/j.tecto.2013.09.030